Regular Article

Quantitative spectral micro-CT of a CA4+ loaded osteochondral sample with a tabletop system

Simone Fantoni[1], Francesco Brun[2,3], Paolo Cardarelli[4,a], Fabio Baruffaldi[1], Virginia Cristofori[5], Angelo Taibi[4,6], Claudio Trapella[5], Luca Brombal[3,7,b]

[1] Medical Technology Laboratory, IRCCS Istituto Ortopedico Rizzoli, via di Barbiano 1/10, 40136 Bologna, Italy
[2] Department of Engineering and Architecture, University of Trieste, via A. Valerio 10, 34127 Trieste, Italy
[3] INFN, Division of Trieste, via A. Valerio 2, 34127 Trieste, Italy
[4] INFN, Division of Ferrara, via G. Saragat 1, 44122 Ferrara, Italy
[5] Department of Chemical, Pharmaceutical and Agricultural Sciences, University of Ferrara, via Luigi Borsari 46, 44121 Ferrara, Italy
[6] Department of Physics and Earth Science, University of Ferrara, via G. Saragat 1, 44122 Ferrara, Italy
[7] Department of Physics, University of Trieste, via A. Valerio 2, 34127 Trieste, Italy

Abstract Micro-computed tomography (μCT) is the gold standard for nondestructive 3D imaging of biomedical samples in the centimeter scale, but it has limited effectiveness in revealing intricate soft tissue details due to the limited attenuation contrast. Radiopaque contrast agents that accumulate in the structures of interest are employed to enhance their visibility. However, the increased attenuation provided by the contrast agents does not guarantee discrimination among tissues. This issue can be solved by spectral μCT (SμCT) systems employing small-pixel chromatic photon-counting detectors. These detectors, combined with material decomposition algorithms, allow the generation of high-resolution material-specific 3D maps. This work aims to demonstrate the potential of photon-counting X-ray SμCT on osteochondral samples loaded with a cationic iodinated contrast agent (CA4+) at a spatial resolution below 50 μm, and to compare the results against a conventional μCT system. An osteochondral sample extracted from a bovine stifle joint was loaded with CA4+ and imaged with a novel multimodal X-ray imaging system, featuring a 62 μm pixel CdTe spectral detector (Pixirad1-PixieIII). After material decomposition, quantitative 3D density maps of iodine and hydroxyapatite were reconstructed. The same sample was also scanned with a commercial μCT scanner with matched spectrum and exposure time. SCTμ images at a (measured) spatial resolution comparable with the commercial scanner (∼45 μm) were obtained. Spectral images allowed for a fully automatic segmentation of cartilage and subchondral bone. The unambiguous discrimination between iodine and hydroxyapatite revealed a more realistic representation of proteoglycan distribution compared to conventional imaging.

1 Introduction

Articular cartilage (AC) is a soft tissue conferring nearly frictionless and smooth motion at the articular level. The interplay among its constituents, namely collagen, proteoglycans (PGs), and interstitial fluid, delivers excellent mechanical properties to healthy AC [1]. Compositional and morphological modifications of AC, identified as fibrillation of collagen fibers and depletion of PGs, alter the homeostasis of AC with a severe negative impact on its mechanics. As a consequence, progressive wear of AC triggers the onset of joint-affecting diseases such as osteoarthritis [2]. Further hallmarks of AC degeneration are also detected on the subchondral bone, the dense mineralized layer supporting AC in load-bearing events [3]. For these reasons, the availability of imaging tools enabling the identification and monitoring of the progression of osteoarthritis on both AC and subchondral bone is of paramount importance.

Nowadays, X-ray micro-computed tomography (μCT) provides high-spatial resolution 3D reconstructions of biological samples. For advanced systems featuring synchrotron radiation, spatial resolution reaches even the cellular level [4, 5]. Several studies demonstrated that μCT is a powerful tool for the evaluation of mineralized tissues [6]. However, the low radiopacity of AC hinders the evaluation of the progression of the pathological state through μCT. Recently, the adoption of dedicated contrast agents (CAs) allowed advances in terms of qualitative and quantitative assessment of AC. In fact, CAs based on high atomic number (Z) elements, such as iodine and gadolinium, significantly enhance X-ray visualization of soft tissues [7]. Depending on the electrostatic properties of CAs, they can be categorized into non-ionic and ionic CAs. Ionic CAs can be further subdivided into anionic and cationic, if the corresponding molecules host negative or positive charge density, respectively. The ionic nature of CA molecules determines the electrostatic interaction with biological structures [8]. In this context, conventional commercial non-ionic and anionic CAs were

ᵃ e-mail: cardarelli@fe.infn.it (corresponding author)

ᵇ e-mail: lbrombal@units.it (corresponding author)

tested for X-ray visualization of AC, displaying negative or weak correlation to PG content, which exhibits a negative fixed charge density [9]. As a result, high concentrations and long exposure times were required to yield an effective AC imaging [10]. In recent times, dedicated CAs have been developed to improve cartilage visualization, as in the case of cationic iodine-based CA4+ [11]. The positive charge density generates electrostatic attraction between CA4+ molecules and negatively-charged PGs, resulting in shorter diffusion times, lower CA concentrations required, and direct correlation of CA distribution with PG content [10].

Although the use of CAs addresses the poor visibility of the cartilage, contrast-enhanced μCT (CEμCT) still fails in distinguishing tissues exhibiting similar X-ray attenuation, such as contrast-enhanced AC from subchondral bone, potentially hindering their exact segmentation, quantification, and, more generally, a detailed evaluation of osteoarthritis progression [12]. This limitation can be overcome by using X-ray spectral imaging (XSI). XSI relies on measurements at two (or more) X-ray energy levels (or bins) and provides tissue separation by exploiting the different attenuation energy dependence of the CA.

Historically, XSI has been implemented by using dual-energy or multi-energy methods based on acquisitions of the sample performed with different X-ray spectra [13]. This typically implies the use of complex dual source or fast kilovoltage switching systems or, alternatively, requires multiple scans, posing concerns in terms of image registration and, for *in-vivo* applications, of deposited radiation dose [14]. Along with studies based on conventional X-ray tubes, various XSI tests have been carried out at synchrotron facilities for the visualization of AC with different combinations of ionic contrast media [15–18]. Despite the demonstration of high-quality imaging, the peculiar features of synchrotron radiation are hardly reproducible in laboratory-based setups.

The recent advent of photon-counting detectors (PCDs) is going to revolutionize XSI in preclinical and clinical imaging applications, thus overcoming these concerns [19–21]. In fact, the adoption of PCD devices brings a simplification in the hardware and, by employing a broad X-ray spectrum, allows to target applications making use of different contrast media by simply adjusting the energy-calibrated thresholds. The possibility of acquiring images over multiple energy bins in a single shot guarantees exact spatial and temporal registration of spectral images and does not require additional radiation dose [22]. Moreover, with respect to conventional integration devices, the design of PCDs implies advantages in terms of electronic noise suppression (Poisson-dominated noise), artifact suppression, and contrast-to-noise-ratio, the latter due to their intrinsic absence of spectral weighting upon detection [21]. Even more recently, spectral μCT (SμCT) has been made possible by the availability of devices featuring a small pixel size (∼50 μm) and charge-sharing compensation or clustering mechanisms guaranteeing both spectral performance and high-spatial resolution [23, 24].

Focusing on AC applications, previous studies implemented XSI of AC with anionic and non-ionic CAs, exploiting the anti-correlation between their distribution across the tissue and PG content [25, 26]. Cationic CAs were considered for quantitative imaging of AC with dual-energy techniques implemented with indirect conversion detectors by using monochromatic synchrotron radiation [17, 18, 27] and recently with a PCD-based CT system by Paakkari et al. [28], although in the latter attention was drawn exclusively to the assessment of AC and not to the underlying subchondral bone, and the achieved spatial resolution was in the order of 200 μm.

In this framework, our research work demonstrates the potential of SμCT based on a novel system integrating a chromatic PCD (Pixirad1-PixieIII) in the context of osteoarticular imaging at a spatial resolution below 50 μm. Following the treatment to CA4+ targeting PG's structures, osteochondral samples were scanned with scan time and X-ray spectrum, matched to a conventional state-of-the-art μCT scanner. Spectral decomposition has been performed in two basis materials, and imaging performance on the same sample was directly compared to a commercial CEμCT system. Results provide a simultaneous evaluation (both qualitative and quantitative) of cartilage and bone tissues, with the smallest pixel size reported so far referring to a tabletop PCD system, to the best of the authors' knowledge. Noteworthily, the SμCT system allowed a better understanding of the distribution of CA4+ at the bone/CA interface and enabled the automatic segmentation of cartilage and subchondral bone.

2 Materials and methods

2.1 Preparation of sample and contrast agent

The imaged sample was one cylindrical osteochondral plug ($\varnothing = 10$ mm, height$= 10$ mm) extracted from a bovine stifle joint, provided by a local slaughterhouse, and stored in phosphate-buffered saline (PBS) solution-soaked lint at $T = -20°$C. Before the image acquisition, the sample was thawed in PBS solution at $T = 4°$C overnight, inserted in a custom-made polymethyl-metacrylate (PMMA) sample holder and immersed in CA solution [29]. The sample holder had an inner diameter of 10 mm, so that a single cylindrical sample could fit inside, and a height of 30 mm, to fit both the sample and the CA bath.

The used contrast agent was CA4+ (5, 50-[Malonylbis(azanediyl)]bis[N1,N3-bis(2-aminoethyl)-2, 4, 6-triiodoisophthalamide] chloride), which contains six iodine atoms per molecule. The net positive charge ($q = +4$ per molecule) confers the characteristic affinity of CA4+ to PGs, which have instead a negative fixed charge density. CA4+ salts were synthesized according to the work of Stewart et al. [30], and dissolved in PBS solution to reach the desired iodine concentration of 10 mgI/ml. The pH of the resulting aqueous compound was balanced to 7.4 by adding NaOH 4 M. The CA4+ solution was poured on the surface of the cartilage tissue after the insertion of the plug in the sample holder. In addition to the 10 mgI/ml solution, three other CA4+ solutions, with

Fig. 1 Photograph of the SµCT experimental setup at PEPILab. The inset shows a zoomed image of the osteochondral sample where its main components are outlined
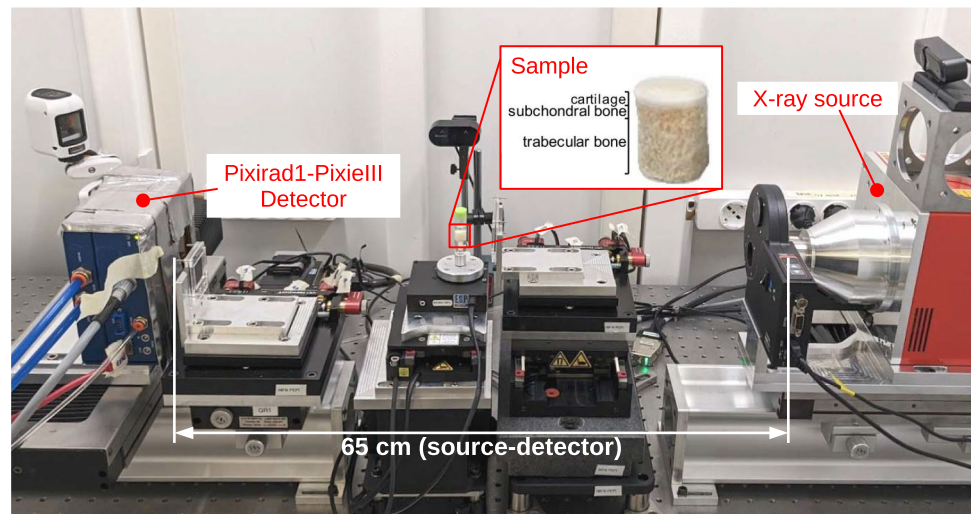
iodine concentrations of 20 mgI/ml, 15 mgI/ml, 5 mgI/ml, and 0 mgI/ml (pure water), respectively, were prepared and used for the calibration of the SµCT system.

2.2 µCT acquisition

SµCT acquisitions were performed at the multipurpose X-ray laboratory PEPILab [31] at the Italian National Institute for Nuclear Physics (INFN) in Trieste: the experimental setup used for the acquisition is shown in Fig. 1. X-rays are produced by a conventional microfocus source (Hamamatsu L10101), operated at 50 kV and 200 µA. A filtration of 0.12 mm of Cu and 0.2 mm of Al was introduced, resulting in a spectrum peaked at the iodine K-edge energy (33.2 keV). From previous characterization measurements, the focal spot size was estimated to be 16 ± 3 µm for the used voltage and current settings [31]. The used chromatic PCD is a Pixirad1-PixieIII, featuring a 62 µm pixel size and a sensitive area of 512×402 pixels, corresponding to 31.7×24.9 mm^2 [24].

The overall source-to-detector distance was set to 65 cm, while geometric magnification was 1.83, corresponding to a reconstruction voxel size of 34 µm and a field-of-view of 17.2×13.7 mm^2. The detector was operated in the charge-summing mode that compensates for the effect of charge sharing and optimizes the intrinsic spatial resolution, corresponding to the dimension of one pixel [32]. Spectral images were generated by using the two-color mode, which yields two independent images corresponding to low and high-energy bins. Bins are defined by two energy-calibrated thresholds, which were set to 26 keV and 33 keV. The second threshold was chosen to maximize the iodine signal, while the first was adjusted to reject the cadmium fluorescence (K_α at 23.2 keV), hence reducing the spectral cross-talk between energy bins. It should be noted that in a CdTe sensor also tellurium fluorescence is produced. However, it is locally self-absorbed in the sensor with high probability as its energy (K_α at 27.5 keV) is just above the cadmium K-edge (26.7 keV) [32]. Exposure time was set to 7.2 s per projection and 1000 projections were acquired over a 360-degree rotation, corresponding to an overall acquisition time of 120 min. No relevant polarization time-dependent effects [33] were observed during the acquisition, owing to the relatively low X-ray flux (order of 500 photons/pixel/s) and the fast polarization/depolarization cycles between consecutive projections enabled by the step-and-shoot acquisition procedure. A random jittering motion of the detector was introduced in between projections to mitigate ring artifacts [34].

In addition to the osteochondral sample, two calibration phantoms were imaged to achieve accurate quantification of iodine concentration and bone density. The first was an epoxy resin phantom (QRM, Moehrendorf, Germany) containing five inserts with different hydroxyapatite (HA) densities. The second was custom-made phantom including five cuvettes filled with different concentrations of CA+, as described in the previous section.

After the spectral scan, the same osteochondral core was acquired with a commercial µCT system (Skyscan 1072, SkyScan, Aartselaar, Belgium) at the Medical Technology Laboratory of Istituto Ortopedico Rizzoli in Bologna. Between acquisitions ($\sim$ 48 h), the sample was stored in CA4+ solution at $T = 4°$C. CEµCT acquisitions were performed with the parameters routinely used for osteochondral samples. The X-ray tube was operated at a voltage of 50 kV and 200 µ A (as for the SµCT scan) with an added filtration of 1 mm-Al. 410 projections over 185° were acquired with an exposure time of 11.8 s per frame, leading to a total scan time (including dead time) of 112 min, which is comparable to the SµCT scan. Given the similar X-ray beam quality, total exposure time and source-to-sample distance of SµCT and commercial CEµCT, the number of projections used matched the integrated fluence at the sample. Images were collected with an energy-integrating detector (Hamamatsu C4742-55), consisting of a CCD camera coupled to a scintillator. The CCD array features a pixel size of 6.7 µm, and an active area of 1024×1024 pixels. The scintillator is coupled to the sensor with optical fibers and a 3.7:1 size ratio. Provided a source-to-detector distance of 84 cm and geometric magnification of 2.2, the final reconstruction voxel size was 11.5 µm and the field-of-view 11.8×11.8 mm^2.

Fig. 2 HA (**a**) and iodine (**b**) density maps of the two calibration phantoms, respectively. In (**c**) and (**d**), the respective measured against nominal density values and the linear fit functions. Fit parameters and associated uncertainties are reported in the plots
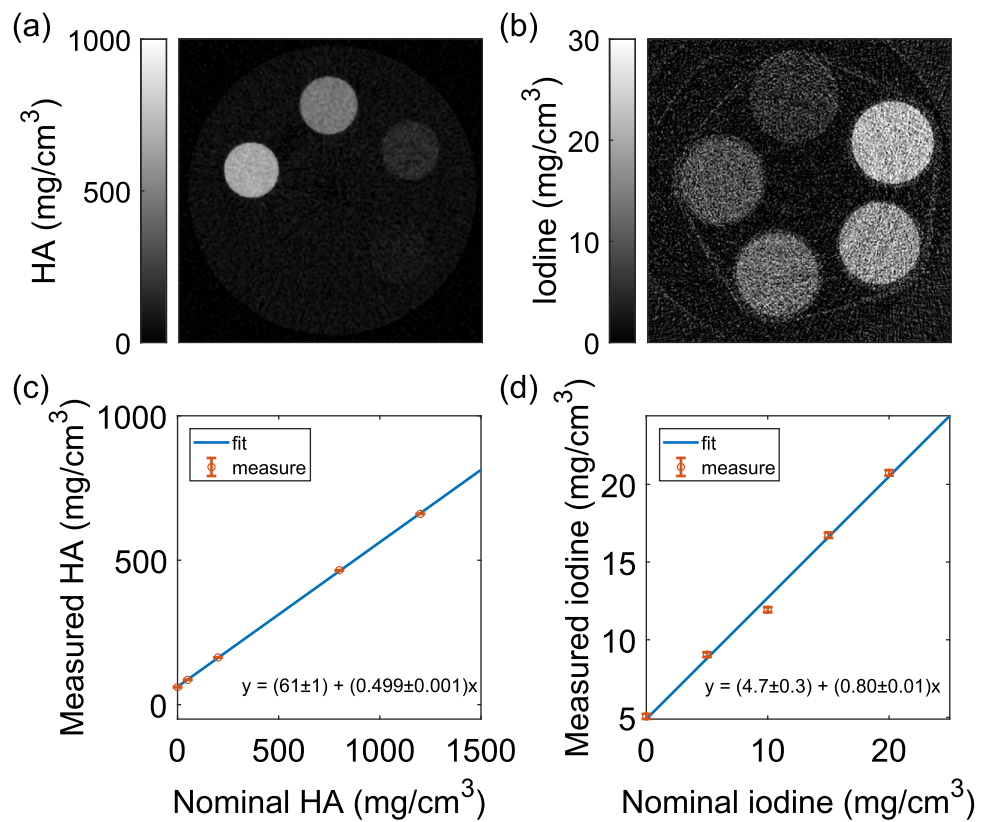

2.3 Calibration, data processing, and analysis

High- and low-energy projection images of the two calibration phantoms underwent a dedicated preprocessing procedure to mitigate detector-specific artifacts [35]. Preprocessed projections were reconstructed via conventional cone-beam FDK [36] with Shepp-Logan filtering, by using the implementation available in the open-source software library TIGRE [37]. Spectral basis material decomposition was performed on the 3D reconstructed volumes through matrix inversion. The mass attenuation coefficient system matrix accounts for the X-ray spectrum and the detector spectral response (including fluorescence), which is obtained with an experimentally validated custom simulation software [38, 39]. The basis materials chosen for the decomposition of the two phantoms were HA and iodine. From the resulting HA and iodine maps, shown in Fig. 2 a and b, mean densities were measured from circular areas within the inserts/cuvettes and plotted against their nominal value. Uncertainty on the measured data was calculated as the standard error of the mean. Data were fitted with a linear function, whose parameters are used to calibrate the osteochondral sample's images. Calibration results are reported in Fig. 2 c and d.

The osteochondral sample's data followed the same pipeline described for the calibration phantom except for the addition of a self-supervised deep denoising procedure that is applied to reconstructed datasets [35]. This processing step is carried out to mitigate noise amplification occurring in the following spectral decomposition step [40]. Consistently with the calibration, the materials chosen for the spectral decomposition of the osteochondral core were iodine and HA, for cartilage and bone tissues, respectively. The former element accounts for the radiopacity of CA4+ targeting PGs in the cartilage tissue. The latter is a mineral constituent of bone tissue and hosts calcium as its radiopaque counterpart. As a result, mass density 3D maps of iodine and HA were obtained from the reconstructed volumes. To carry out the direct comparison with CEμCT, a non-spectral attenuation reconstruction was produced by summing high- and low-energy projections prior to processing. The availability of spectrally decomposed volumes allowed for the implementation of an automatic segmentation procedure for separating bone and cartilage based on the Otsu thresholding algorithm [41]. The obtained volumetric masks were then applied on both (non-spectral) attenuation and material decomposition volumes.

The CEμCT reconstruction was performed by using the manufacturer's software (NRecon, Skyscan, Aartselaar, Belgium). Since the two scans feature different voxel sizes and detector technologies, the spatial resolution has been estimated from the reconstructed images for both CEμCT and (attenuation) SμCT scans. Spatial resolution was evaluated by fitting with an error function (erf) the intensity profile obtained across a sharp bone detail, and defined as the full width at half maximum (FWHM) of the Gaussian obtained deriving the erf fit. Additionally, to apply the same segmentation masks on the CEμCT image, the reconstructed attenuation volumes were co-registered. The registration of volumes was performed in Matlab, by using the function *imregister*. Among the possible registration methods, the similarity criterion was selected, which allows for rotation, translation and dilation of target volume

Fig. 3 Section of reconstructed volume from CEμCT (**a**) and from SμCT (**b**). In both sections, the three main layers of the osteochondral plug, namely CA4+ bath, cartilage, and bone are highlighted. In the bottom panels, the line profiles for CEμCT (**c**) and SμCT (**d**) are reported together with the erf fit. Profiles are extracted from the yellow line ROI drawn in (**a**) and (**b**), respectively, pointed out by the arrows
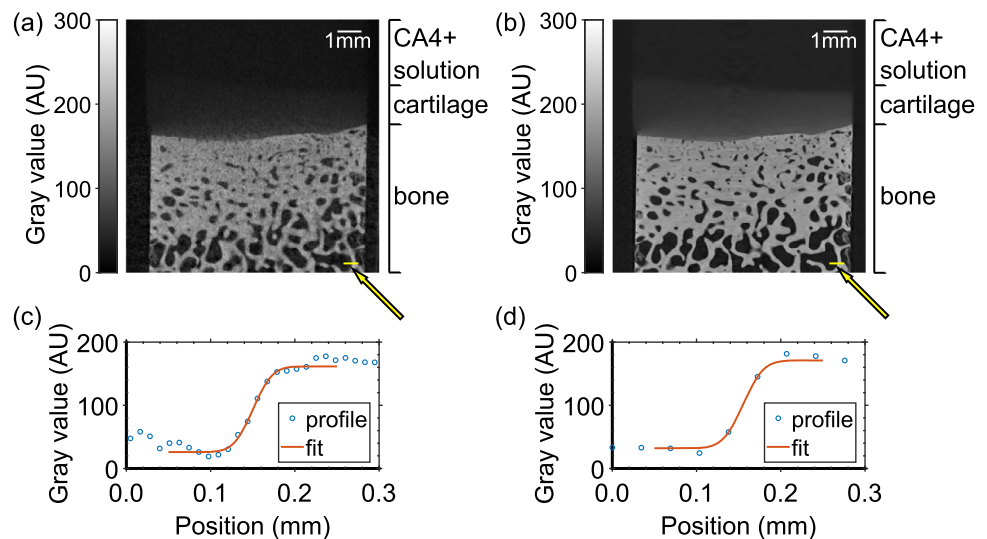
(CEμCT) to the reference volume (SμCT). The metrics used is the *mean square difference* and the optimizer is *regular step gradient descent*. The results of the registration were evaluated by visual inspection of the voxel-by-voxel subtraction of the registered and target volumes.

After registration, the depth-wise intensity concentration profiles across the cartilage were extracted and compared for both attenuation images obtained with the two systems and for the iodine decomposed image of the SμCT system. Attention was focused on the differences between attenuation and iodine density (i.e., PG) distributions close to the AC tidemark, which is the narrow region of interface between calcified cartilage and subchondral bone. In fact, modifications to the cartilage tidemark can be considered as a hallmark for recognition of osteoarticular pathologies like osteoarthritis [3]. For this reason, the tidemark voxels of all the images were realigned to a planar surface via translation in order to study the profiles across the whole volume as a function of the distance from the cartilage-bone interface. The tidemark position for each voxel column was identified as the first pixel separating the subchondral bone from the segmented volume of cartilage.

3 Results

One transverse slice obtained from the CEμCT reconstruction and the corresponding detail from the (nonspectral) attenuation volume obtained with the SμCT are reported in Fig. 3. In both images, three layers of the sample are fairly visible, corresponding (from top to bottom) to the CA4+ bath, the contrast-enhanced cartilage, and the underlying bone tissue. As demonstrated by the line profiles across a sharp bone detail, the spatial resolution of the two systems is similar and the FWHM is estimated to be 45 ± 15 μm for the SμCT and 43 ± 15 μm for the CEμCT, where uncertainties correspond to the 95% confidence level given by the fitting procedure.

The same transverse slice reconstructed from the high- and low-energy bins of the SμCT dataset is shown in panels (a) and (b) of Fig. 4. From the images, it is clear that, while the bone tissue signal decreases at high energy, the cartilage signal has an opposite behavior due to the presence of CA4+. Panels (c) and (d) show the iodine and HA mass density maps after spectral decomposition and automatic segmentation.

The intensity distributions across the cartilage volumes obtained from the CEμCT, (non-spectral) attenuation SμCT, and the iodine mass density distribution obtained from the SμCT are shown in panels (a) to (c) of Fig. 5, respectively.

Their respective normalized intensity profiles are reported in panels (d) to (f). From the profiles, it can be noted that, regardless of the system used, attenuation-only μCT images have a signal peaked at the bone/cartilage interface, while the spectral image reveals an iodine peaking approximately 150 μm above the interface. Albeit this value can be affected by possible misregistration errors (order of 1 pixel), the fact that the shift in the peak appears systematically across the whole volume indicates a clear difference between the SμCT and CEμCT profiles.

Starting from material decomposition volumes, a 3D rendering of the scanned sample was also produced, as shown in Fig. 6. The CA4+ perfused cartilage has been rendered in blue, where a darker color is related to a higher concentration, while the underlying bone structure is rendered with a light brown palette.

Fig. 4 Section of the reconstructed volume of laboratory SµCT, taken from low-energy (**a**) and high-energy bins reconstructions (**b**). Spectral decomposition in iodine (**c**) and HA basis (**d**) after the application of the automatic segmentation
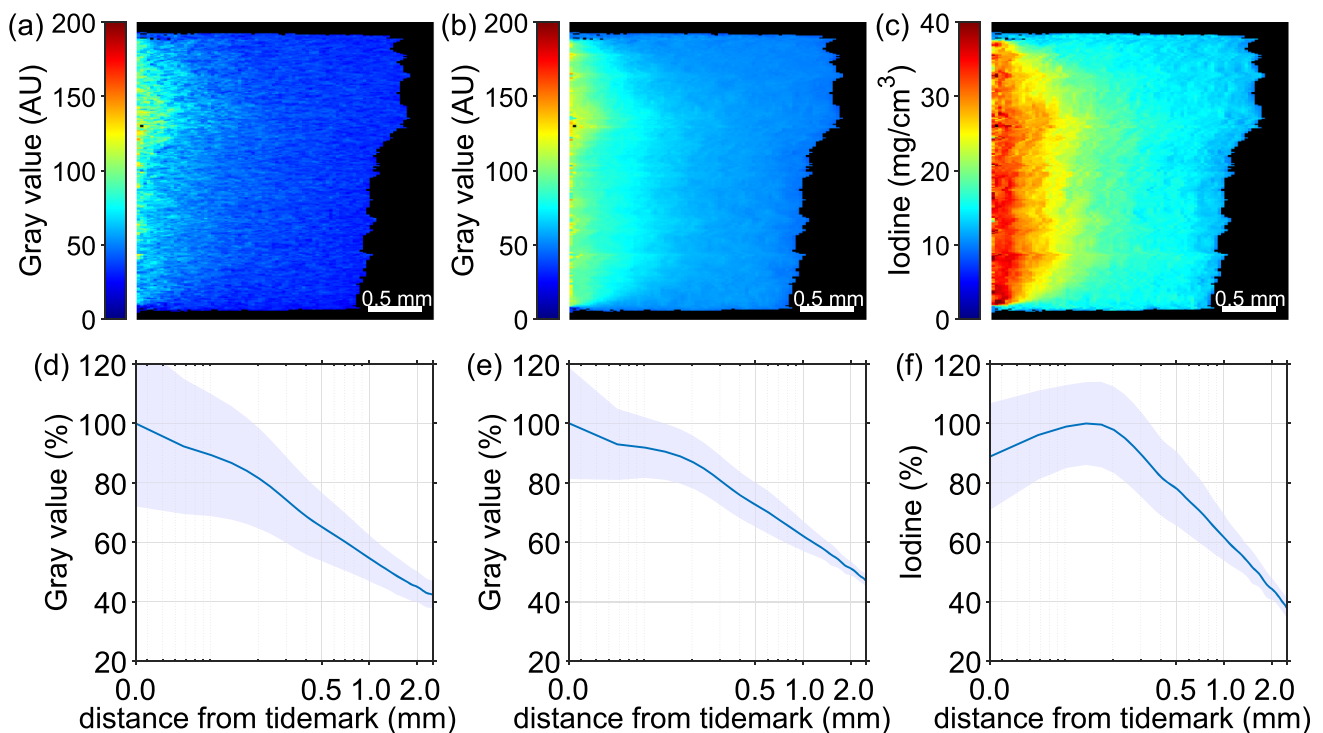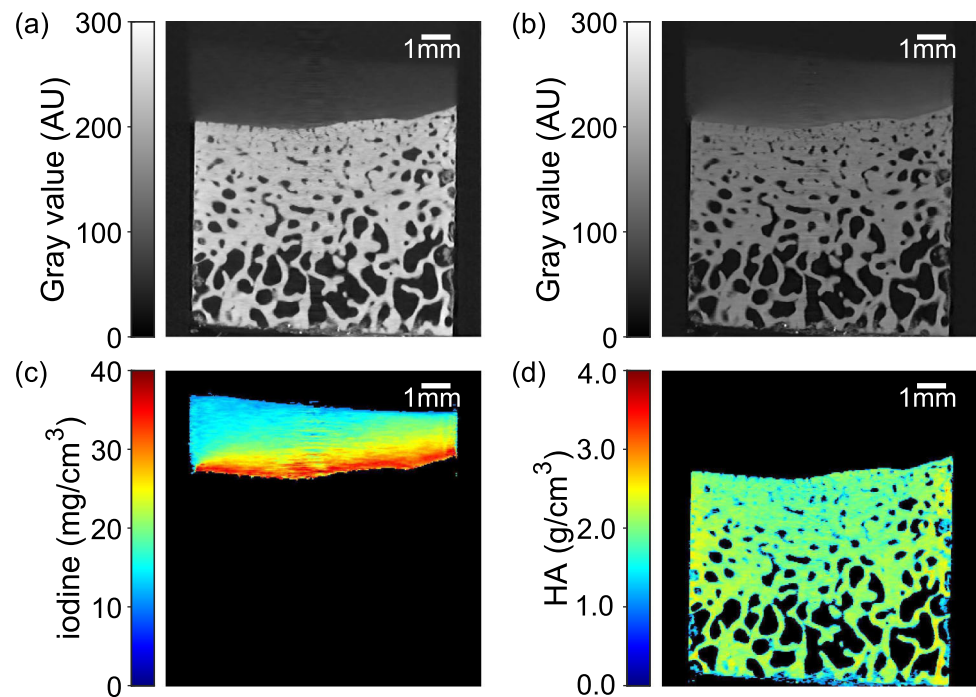

Fig. 5 Sections from volumes realigned to a planar tidemark surface, from CEµCT (**a**), and absorption (**b**) and iodine-base decomposition (**c**) from SµCT. Their respective intensity profiles (solid lines), corresponding to the volume average as a function of the distance from the tidemark, are shown in (**d**), (**e**), and (**f**). Similarly, for each profile, the data dispersion (shaded area) corresponds to one standard deviation. For comparison, each profile is normalized to its maximum value. The distance from the tidemark position (0 mm) is reported in logarithmic scale in plots (**d**), (**e**), and (**f**)

4 Discussion

Given similar parameters in terms of acquisition time and X-ray spectrum, a qualitative comparison between the conventional CEµCT and the (non-spectral) attenuation images acquired with the SµCT reveals comparable results in terms of image appearance, as seen in Fig. 3. This also demonstrates that the sample was not significantly altered in the time elapsed between the two scans (48 h).

Fig. 6 3D rendering of the sample acquired with the SµCT system. The blue palette displays iodine content (darker at higher concentrations), the light brown palette displays the HA distribution
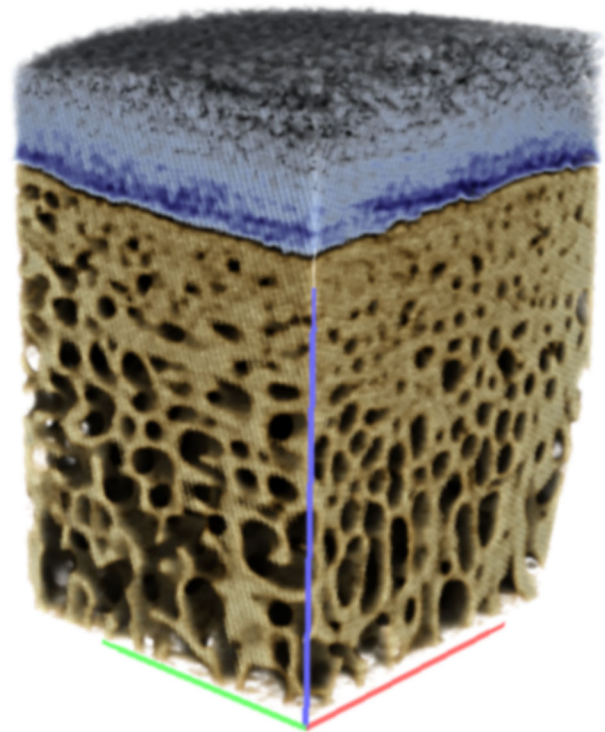
Quantitatively, the two systems revealed a similar spatial resolution in the order of 45µm, despite a factor of 3 difference in voxel size. This is related to the high efficiency and sharp response of the PCD detector used in the SµCT. In both scans, features within the mineralized tissue, namely the characteristic trabeculae found in cancellous bone, could be easily distinguished. On the other hand, even if the SµCT image shows a generally higher image quality, the interface between cartilage and CA4+ remained ambiguous. The same observation holds for the interface between cartilage tissue and subchondral bone.

This limitation is overcome by spectral images delivered by the SµCT. A higher intensity of dense structures is found in the low-energy channel with respect to the high-energy one, while the opposite behavior is observed in the presence of iodine. This allows for the discrimination between the cartilage and the mineralized tissue as well as for masking out the CA4+ bath that contains a lower iodine concentration with respect to the cartilage, as reported in panel (c) of Fig. 4. Moreover, further quantitative examination of bone tissue, based on quantification of the mineral density, is promptly accessible in spectral modality, as shown in panel (d), while calibration curves are required in attenuation modality.

Focusing on the cartilage layer, a depth-wise intensity/concentration dependence could be observed, generally decreasing from the deep cartilage, rich in PG, to the superficial layer, as demonstrated in Fig. 5. Noteworthily, the comparison between profiles from absorption and spectral imaging outlines the potential of material decomposition. In particular, while the attenuation-based CTs show a similar monotonically decreasing behavior regardless of the used imaging system, the peak in the spectral density profile is shifted with respect to the bone/cartilage interface. This is due to the fact that only the spectral decomposition can discriminate between different contributions to the attenuation at the cartilage tidemark, distinguishing between the iodine, related to PG concentration, and the calcified tissue. From a biological perspective, the PG distribution shown in the material decomposition can be understood by considering that the cartilage tissue close to the tidemark shows increased content of calcification, at the expense of PG concentration. These results are consistent with previous literature. The work of Bansal et al. [10] demonstrated the correlation between CA4+ uptake and GAG overall content in the cartilage in bovine osteochondral samples from the femoral condyles. The 3D CA4+ distribution reported in their study showed a clear gradient, with increasing CA uptake in the deeper layer of cartilage. Similarly, the work by Honkanen et al [17] performed on human cadaver samples showed that, at diffusion equilibrium (72 h of immersion), CA4+ distribution at increasing depths in the cartilage correlates with PG concentration. The hypothesis that the PG concentration decreases in calcified cartilage close to the tidemark is supported in the literature by independent methods, which provided direct measurements of thickness of calcified cartilage. Values of the order of 200 µm were found in Kauppinen et al. [42], by segmenting histological images from healthy human tissues.

In this context, the calcium quantification capabilities enabled by SµCT, could provide a powerful tool for the nondestructive 3D assessment of the calcified cartilage region. Indeed, the simultaneous but differentiated assessment of cartilage and subchondral bone is considered to be of great importance for the understanding of pathologies such as osteoarthritis, which concurrently develops in both tissues [3]. In previous works, the use of cationic CA4+ for the evaluation of cartilage tissue [43] was extensively validated using reference methods [44], conventional CT, and synchrotron µCT [27, 45–47], but it was faced with the problem of comparable

radiopacity of contrast-enhanced cartilage and calcified tissue [12]. This further implies that manual segmentation procedures are typically used for the delineation of articulating surfaces and cartilage-bone surfaces [15–18], potentially being imprecise and/or subject to operator-dependent bias. On the other hand, spectral data-based material decomposition enables the automatic segmentation of heterogeneous structures as demonstrated, for instance, in the 3D rendering of Fig. 6.

Despite only few studies making use of detector-based spectral systems have been reported in the literature on osteochondral samples, those works focused either on the diffusion of anionic CAs, which anticorrelates with PG [25], or on PG-affine CA4+ but at a much coarser spatial resolution (order of 200 μm) [28]. In this framework, to the best of the authors' knowledge, our work reports the first SμCT on an osteochondral sample loaded with an iodine-based cationic contrast agent to be scanned with a laboratory spectral PCD system at a (measured) spatial resolution below 50 μm.

It is understood that the promising results demonstrated in this paper have been obtained on a single sample, and need to be confirmed on a larger number of samples. This should also account for the fact that the features in the articular cartilage strongly depend on the location in articulating sites [48], hence differences in morphology (i.e., thickness) and composition (i.e., PG content) might impact the imaging outcome. Another limitation of the study is the simplified (cylindrical) geometry of osteochondral samples. In fact, the relatively small size and constrained geometry might overestimate the potential of automatic segmentation provided by spectral imaging. A comprehensive evaluation should include samples with complex geometries and greater size or, alternatively, whole-sized condyles from small animal models.

5 Conclusion

The present study investigated the potential of the SμCT on an osteochondral sample perfused with the iodine-based cationic contrast agent CA4+ and compared the results against a commercial CEμCT system. For similar acquisition time and spectrum, the results demonstrate that the SμCT provides a better distinction among tissues, also enabling automatic segmentation, at comparable spatial resolution. Spectral capabilities allowed for a more realistic description of proteoglycan distribution across the cartilage. The material decomposition approach makes possible the unambiguous discrimination between iodine and hydroxyhapatite at the cartilage/bone interface, having a potential impact for the assessment of osteoarticular pathologies. Future studies will be aimed at extending the analysis to a larger number of samples and sample types, while further improving spatial resolution (by a factor between 1.5 and 2) using a higher magnification and the extended field-of-view acquisition modality.

References

1. V.C. Mow, A. Ratcliffe, A.R. Poole, Cartilage and diarthrodial joints as paradigms for hierarchical materials and structures. Biomaterials **13**(2), 67–97 (1992). https://doi.org/10.1016/0142-9612(92)90001-5
2. J. Martel-Pelletier, Pathophysiology of osteoarthritis. Osteoarthr. Cartil. **12**, 31–33 (2004). https://doi.org/10.1016/j.joca.2003.10.002
3. S.R. Goldring, M.B. Goldring, Changes in the osteochondral unit during osteoarthritis: structure, function and cartilage-bone crosstalk. Nat. Rev. Rheumatol. **12**(11), 632–644 (2016). https://doi.org/10.1038/nrrheum.2016.148
4. M. Fratini, I. Bukreeva, G. Campi, F. Brun, G. Tromba, P. Modregger, D. Bucci, G. Battaglia, R. Spanò, M. Mastrogiacomo, H. Requardt, F. Giove, A. Bravin, A. Cedola, Simultaneous submicrometric 3D imaging of the micro-vascular network and the neuronal system in a mouse spinal cord. Sci. Rep. **5**(1), 8514 (2015). https://doi.org/10.1038/srep08514
5. L. Massimi, I. Bukreeva, G. Santamaria, M. Fratini, A. Corbelli, F. Brun, S. Fumagalli, L. Maugeri, A. Pacureanu, P. Cloetens, N. Pieroni, F. Fiordaliso, G. Forloni, A. Uccelli, N. Kerlero De Rosbo, C. Balducci, A. Cedola, Exploring Alzheimer's disease mouse brain through X-ray phase contrast tomography: From the cell to the organ. NeuroImage **184**, 490–495 (2019). https://doi.org/10.1016/j.neuroimage.2018.09.044

6. M.P. Akhter, R.R. Recker, High resolution imaging in bone tissue research-review. Bone **143**, 115620 (2021). https://doi.org/10.1016/j.bone.2020.115620

7. A.W. Palmer, R.E. Guldberg, M.E. Levenston, Analysis of cartilage matrix fixed charge density and three-dimensional morphology via contrast-enhanced microcomputed tomography. Proceedings of the National Academy of Sciences of the United States of America **103**(51), 19255–19260 (2006). https://doi.org/10.1073/pnas.0606406103

8. H. Lusic, M.W. Grinstaff, X-ray-computed tomography contrast agents. Chem. Rev. **113**(3), 1641–1666 (2013). https://doi.org/10.1021/cr200358s

9. S. De Bournonville, S. Vangrunderbeeck, G. Kerckhofs, Contrast-enhanced MicroCT for virtual 3D anatomical pathology of biological tissues: a literature review. Contrast Media Mol. Imagin. **2019**, 1–9 (2019). https://doi.org/10.1155/2019/8617406

10. P.N. Bansal, R.C. Stewart, V. Entezari, B.D. Snyder, M.W. Grinstaff, Contrast agent electrostatic attraction rather than repulsion to glycosaminoglycans affords a greater contrast uptake ratio and improved quantitative CT imaging in cartilage. Osteoarthr. Cartil. **19**(8), 970–976 (2011). https://doi.org/10.1016/j.joca.2011.04.004

11. N.S. Joshi, P.N. Bansal, R.C. Stewart, B.D. Snyder, M.W. Grinstaff, Effect of contrast agent charge on visualization of articular cartilage using computed tomography: exploiting electrostatic interactions for improved sensitivity. J. Am. Chem. Soc. **131**(37), 13234–13235 (2009). https://doi.org/10.1021/ja9053306

12. L. Xie, A.S.P. Lin, M.E. Levenston, R.E. Guldberg, Quantitative assessment of articular cartilage morphology via EPIC-μ CT . Osteoarthr. Cartil. **17**(3), 313–320 (2009). https://doi.org/10.1016/j.joca.2008.07.015

13. L.A. Lehmann, R.E. Alvarez, A. Macovski, W.R. Brody, N.J. Pelc, S.J. Riederer, A.L. Hall, Generalized image combinations in dual KVP digital radiography. Med. Phys. **8**(5), 659–667 (1981). https://doi.org/10.1118/1.595025

14. E. Fredenberg, Spectral and dual-energy X-ray imaging for medical applications. Nucl. Instrum. Method Phys. Res. Sect. A: Accel. Spectrom. Detect. Assoc. Equip. **878**, 74–87 (2018). https://doi.org/10.1016/j.nima.2017.07.044

15. A. Bhattarai, J.T.J. Honkanen, K.A.H. Myller, M. Prakash, M. Korhonen, A.E.A. Saukko, T. Virén, A. Joukainen, A.N. Patwa, H. Kröger, M.W. Grinstaff, J.S. Jurvelin, J. Töyräs, Quantitative dual contrast CT technique for evaluation of articular cartilage properties. Annal. Biomed. Eng. **46**(7), 1038–1046 (2018). https://doi.org/10.1007/s10439-018-2013-y

16. A. Bhattarai, B. Pouran, J.T.A. Mäkelä, R. Shaikh, M.K.M. Honkanen, M. Prakash, H. Kröger, M.W. Grinstaff, H. Weinans, J.S. Jurvelin, J. Töyräs, Dual contrast in computed tomography allows earlier characterization of articular cartilage over single contrast. J. Orthop. Res. **38**(10), 2230–2238 (2020). https://doi.org/10.1002/jor.24774

17. M.K.M. Honkanen, A.E.A. Saukko, M.J. Turunen, R. Shaikh, M. Prakash, G. Lovric, A. Joukainen, H. Kröger, M.W. Grinstaff, J. Töyräs, Synchrotron MicroCT reveals the potential of the dual contrast technique for quantitative assessment of human articular cartilage composition. J. Orthop. Res. **38**(3), 563–573 (2020). https://doi.org/10.1002/jor.24479

18. M.K.M. Honkanen, A.E.A. Saukko, M.J. Turunen, W. Xu, G. Lovric, J.T.J. Honkanen, M.W. Grinstaff, V.-P. Lehto, J. Töyräs, Triple contrast CT method enables simultaneous evaluation of articular cartilage composition and segmentation. Annal. Biomed. Eng. **48**(2), 556–567 (2020). https://doi.org/10.1007/s10439-019-02362-6

19. T. Flohr, M. Petersilka, A. Henning, S. Ulzheimer, J. Ferda, B. Schmidt, Photon-counting CT review. Phys. Med. **79**, 126–136 (2020). https://doi.org/10.1016/j.ejmp.2020.10.030

20. M.J. Willemink, M. Persson, A. Pourmorteza, N.J. Pelc, D. Fleischmann, Photon-counting CT: technical principles and clinical prospects. Radiology **289**(2), 293–312 (2018). https://doi.org/10.1148/radiol.2018172656

21. S.S. Hsieh, S. Leng, K. Rajendran, S. Tao, C.H. McCollough, Photon counting CT: clinical applications and future developments. IEEE Trans. Radiat. Plasma Med. Sci. **5**(4), 441–452 (2021). https://doi.org/10.1109/TRPMS.2020.3020212

22. F. Brun, V. Di Trapani, J. Albers, P. Sacco, D. Dreossi, L. Brombal, L. Rigon, R. Longo, A. Mittone, C. Dullin, A. Bravin, P. Delogu, Single-shot K-edge subtraction x-ray discrete computed tomography with a polychromatic source and the Pixie-III detector. Phys. Med. Biol. **65**(5), 055016 (2020). https://doi.org/10.1088/1361-6560/ab7105

23. R. Ballabriga, J. Alozy, G. Blaj, M. Campbell, M. Fiederle, E. Frojdh, E.H.M. Heijne, X. Llopart, M. Pichotka, S. Procz, L. Tlustos, W. Wong, The Medipix3RX: a high resolution, zero dead-time pixel detector readout chip allowing spectroscopic imaging. J. Instrum. **8**(02), 02016–02016 (2013). https://doi.org/10.1088/1748-0221/8/02/C02016

24. R. Bellazzini, A. Brez, G. Spandre, M. Minuti, M. Pinchera, P. Delogu, P.L. De Ruvo, A. Vincenzi, PIXIE III: a very large area photon-counting CMOS pixel ASIC for sharp X-ray spectral imaging. J. Instrum. **10**(01), 01032–01032 (2015). https://doi.org/10.1088/1748-0221/10/01/C01032

25. K. Rajendran, C. Löbker, B.S. Schon, C.J. Bateman, R.A. Younis, N.J.A. Ruiter, A.I. Chernoglazov, M. Ramyar, G.J. Hooper, A.P.H. Butler, T.B.F. Woodfield, N.G. Anderson, Quantitative imaging of excised osteoarthritic cartilage using spectral CT. Eur. Radio. **27**(1), 384–392 (2017). https://doi.org/10.1007/s00330-016-4374-7

26. K. Baer, S. Kieser, B. Schon, K. Rajendran, T. Ten Harkel, M. Ramyar, C. Löbker, C. Bateman, A. Butler, A. Raja, G. Hooper, N. Anderson, T. Woodfield, Spectral CT imaging of human osteoarthritic cartilage via quantitative assessment of glycosaminoglycan content using multiple contrast agents. APL Bioeng. **5**(2), 026101 (2021). https://doi.org/10.1063/5.0035312

27. A.E.A. Saukko, M.J. Turunen, M.K.M. Honkanen, G. Lovric, V. Tiitu, J.T.J. Honkanen, M.W. Grinstaff, J.S. Jurvelin, J. Töyräs, Simultaneous quantitation of cationic and non-ionic contrast agents in articular cartilage using synchrotron MicroCT imaging. Sci. Rep. **9**(1), 7118 (2019). https://doi.org/10.1038/s41598-019-43276-6

28. P. Paakkari, S.I. Inkinen, M.K.M. Honkanen, M. Prakash, R. Shaikh, M.T. Nieminen, M.W. Grinstaff, J.T.A. Mäkelä, J. Töyräs, J.T.J. Honkanen, Quantitative dual contrast photon-counting computed tomography for assessment of articular cartilage health. Sci. Rep. **11**(1), 5556 (2021). https://doi.org/10.1038/s41598-021-84800-x

29. S. Fantoni, I. Gabucci, P. Cardarelli, G. Paternò, A. Taibi, V. Cristofori, C. Trapella, A. Bazzani, M. Assenza, A. Zanna Bonacorsi, D. Conti, F. Baruffaldi, A cationic contrast agent in X-ray imaging of articular cartilage: pre-clinical evaluation of diffusion and attenuation properties. Diagnostics **12**(9), 2111 (2022). https://doi.org/10.3390/diagnostics12092111

30. R.C. Stewart, A.N. Patwa, H. Lusic, J.D. Freedman, M. Wathier, B.D. Snyder, A. Guermazi, M.W. Grinstaff, Synthesis and preclinical characterization of a cationic iodinated imaging contrast agent (CA4+) and its use for quantitative computed tomography of ex vivo human hip cartilage. J. Med. Chem. **60**(13), 5543–5555 (2017). https://doi.org/10.1021/acs.jmedchem.7b00234

31. L. Brombal, F. Arfelli, R.H. Menk, L. Rigon, F. Brun, PEPI Lab: a flexible compact multi-modal setup for X-ray phase-contrast and spectral imaging. Sci. Rep. **13**(1), 4206 (2023). https://doi.org/10.1038/s41598-023-30316-5

32. V. Di Trapani, A. Bravin, F. Brun, D. Dreossi, R. Longo, A. Mittone, L. Rigon, P. Delogu, Characterization of the acquisition modes implemented in Pixirad-1/Pixie-III X-ray detector: effects of charge sharing correction on spectral resolution and image quality. Nucl. Instrum. Method Phys. Res. Sect. A: Accel. Spectrom. Detect. Assoc. Equip. **955**, 163220 (2020). https://doi.org/10.1016/j.nima.2019.163220

33. L. Brombal, S. Donato, F. Brun, P. Delogu, V. Fanti, P. Oliva, L. Rigon, V. Di Trapani, R. Longo, B. Golosio, Large-area single-photon-counting CdTe detector for synchrotron radiation computed tomography: a dedicated pre-processing procedure. J. Synchrotron Radiat. **25**(4), 1068–1077 (2018).

34. C.K. Hagen, M. Endrizzi, R. Towns, J.A. Meganck, A. Olivo, A preliminary investigation into the use of edge illumination X-ray phase contrast micro-CT for preclinical imaging. Mol. Imagin. Biol. **22**(3), 539–548 (2020). https://doi.org/10.1007/s11307-019-01396-5

35. V. Di Trapani, L. Brombal, F. Brun, Multi-material spectral photon-counting micro-CT with minimum residual decomposition and self-supervised deep denoising. Optics Express **30**(24), 42995 (2022). https://doi.org/10.1364/OE.471439

36. L.A. Feldkamp, L.C. Davis, J.W. Kress, Practical cone-beam algorithm. J. Opt. Soc. Am. A **1**(6), 612 (1984). https://doi.org/10.1364/JOSAA.1.000612

37. A. Biguri, M. Dosanjh, S. Hancock, M. Soleimani, TIGRE: a MATLAB-GPU toolbox for CBCT image reconstruction. Biomed. Phys. Eng. Express **2**(5), 055010 (2016). https://doi.org/10.1088/2057-1976/2/5/055010

38. L. Brombal, L. Rigon, F. Arfelli, R.H. Menk, F. Brun, A Geant4 tool for edge-illumination X-ray phase-contrast imaging. J. Instrum. **17**(01), 01043 (2022). https://doi.org/10.1088/1748-0221/17/01/C01043

39. V. Di Trapani, P. Oliva, F. Arfelli, L. Brombal, R.H. Menk, P. Delogu, Development and validation of a simulation tool for K-edge Subtraction imaging with polychromatic spectra and X-ray photon counting detectors. Nucl. Instrum. Method. Phys. Res. Sect. A: Accel. Spectrom. Detect. Assoc. Equip. **1046**, 167675 (2023). https://doi.org/10.1016/j.nima.2022.167675

40. B. Heismann, B. Schmidt, T. Flohr, Spectral computed tomography. Press monograph / SPIE PM, vol. 226. SPIE Press, Bellingham, Wash (2012)

41. N. Otsu, A threshold selection method from gray-level histograms. IEEE Trans. Syst. Man Cybern. **9**(1), 62–66 (1979). https://doi.org/10.1109/TSMC.1979.4310076

42. S. Kauppinen, S.S. Karhula, J. Thevenot, T. Ylitalo, L. Rieppo, I. Kestilä, M. Haapea, I. Hadjab, M.A. Finnilä, E. Quenneville, M. Garon, H.K. Gahunia, K.P.H. Pritzker, M.D. Buschmann, S. Saarakkala, H.J. Nieminen, 3D morphometric analysis of calcified cartilage properties using micro-computed tomography. Osteoarthr. Cartil. **27**(1), 172–180 (2019). https://doi.org/10.1016/j.joca.2018.09.009

43. M.A. Boos, M.W. Grinstaff, S.R. Lamandé, K.S. Stok, Contrast-enhanced micro-computed tomography for 3D visualization and quantification of glycosaminoglycans in different cartilage types. Cartilage **13**(2–suppl), 486–494 (2021). https://doi.org/10.1177/19476035211053820

44. J.D. Freedman, D.J. Ellis, H. Lusic, G. Varma, A.K. Grant, B.A. Lakin, B.D. Snyder, M.W. Grinstaff, dGEMRIC and CECT comparison of cationic and anionic contrast agents in cadaveric human metacarpal cartilage. J. Orthop. Res.: Official Public. Orthop. Res. Soc. **38**(4), 719–725 (2020). https://doi.org/10.1002/jor.24511

45. B.A. Lakin, D.J. Grasso, S.S. Shah, R.C. Stewart, P.N. Bansal, J.D. Freedman, M.W. Grinstaff, B.D. Snyder, Cationic agent contrast-enhanced computed tomography imaging of cartilage correlates with the compressive modulus and coefficient of friction. Osteoarthr. Cartil. **21**(1), 60–68 (2013). https://doi.org/10.1016/j.joca.2012.09.007

46. R.C. Stewart, P.N. Bansal, V. Entezari, H. Lusic, R.M. Nazarian, B.D. Snyder, M.W. Grinstaff, Contrast-enhanced CT with a high-affinity cationic contrast agent for imaging ex vivo bovine, intact ex vivo rabbit, and in vivo rabbit cartilage. Radiology **266**(1), 141–150 (2013). https://doi.org/10.1148/radiol.12112246

47. A.E.A. Saukko, O. Nykänen, J.K. Sarin, M.J. Nissi, N.C.R. Te Moller, H. Weinans, I.A.D. Mancini, J. Visser, H. Brommer, P.R. Weeren, J. Malda, M.W. Grinstaff, J. Töyräs, Dual-contrast computed tomography enables detection of equine posttraumatic osteoarthritis in vitro. J. Orthop. Res. **40**(3), 703–711 (2022). https://doi.org/10.1002/jor.25066

48. D.R. Pedersen, J.E. Goetz, G.L. Kurriger, J.A. Martin, Comparative digital cartilage histology for human and common osteoarthritis models. Orthop. Res. Rev. **2013**(5), 13–20 (2013). https://doi.org/10.2147/ORR.S38400